CHAPTER 4

ELECTRON BEAM AND ELECTROMAGNETIC WAVES INTERACTION ANALYSIS*

*Part of this work has been published as:

Manpuran Mahto and P. K. Jain, "Electromagnetic Analysis of the HPM Oscillator — Reltron," *AIP Physics of Plasmas*, vol. 23, p. 093118, 2016.

ELECTRON BEAM AND ELECTROMAGNETIC WAVES INTERACTION ANALYSIS

4.1. Introduction

In recent years, considerable research activities have been aroused in the area of the high power microwaves (HPM). Reltron is one of the potential HPM source capable of generating hundreds of megawatt pulsed power in the frequency range of 0.5 GHz to 12 GHz. It is a slow-wave microwave tube derived from the klystron oscillator. A typical reltron schematic is shown in Fig. 4.1 and as described in the previous chapters that the modulation cavity of the device resonates under three different conditions, *i.e.*, 0, $\pi/2$ and π in accordance with their electric field patterns. The desired resonating condition is $\pi/2$, and here, the electron beam gets phase synchronized with the RF waves to produce intense current modulation [Miller *et al*. (1992), Miller *et al*. (1992)]. The experiments for 1 GHz and 3 GHz reltrons which use self-magnetic focussing due to high beam current generated through explosive emission was carried out by Miller *et al*. [Miller *et al*. (1992)]. They have also optimized extraction cavity of the reltron to obtain an RF output energy of 40 Joules per pulse at 3 GHz and frequency agile version of S-band reltron has also been constructed by physically deforming the modulation cavity structure using plungers and tuning screws [Miller *et al*. (1994)]. Miller has briefly described the pulse shortening in the reltron tube and examined the effects of construction material, fabrication techniques, vacuum pressure, and conditioning. To increase the energy per pulse, he used the conventional microwave tube construction techniques, including thermionic cathodes, ceramic insulators, and brazed joining with high-temperature [Miller *et al*. (1998)]. A thermionic emission reltron device has been

studied by Kim *et al.* [Kim *et al*. (1994)] while a dual-mode reltron has been carried out by Soh *et al*. [Soh *et al*. (2012)] using "MAGIC" PIC simulation.

In this chapter, a beam wave interaction process in the reltron device is analyzed starting from the basic principles. The electric field responsible for electron beam bunching process in the side-coupled modulation cavity is presented extending Lemke's concept for split cavity oscillator (SCO) [Lemke (1992)]. The relativistic klystron analysis given by Friedman *et al*. is extended to obtain the beam modulation process in the reltron [Friedman *et al*. (1984), Friedman *et al*. (1988)]. Further, Lemke's analysis is used here to obtain the RF energy developed this device [Lemke (1989)]. Further, in order to evaluate the overall device performance, analytical calculation and simulation using PIC simulation code "CST Particle Studio" using explosive emission model is also performed.

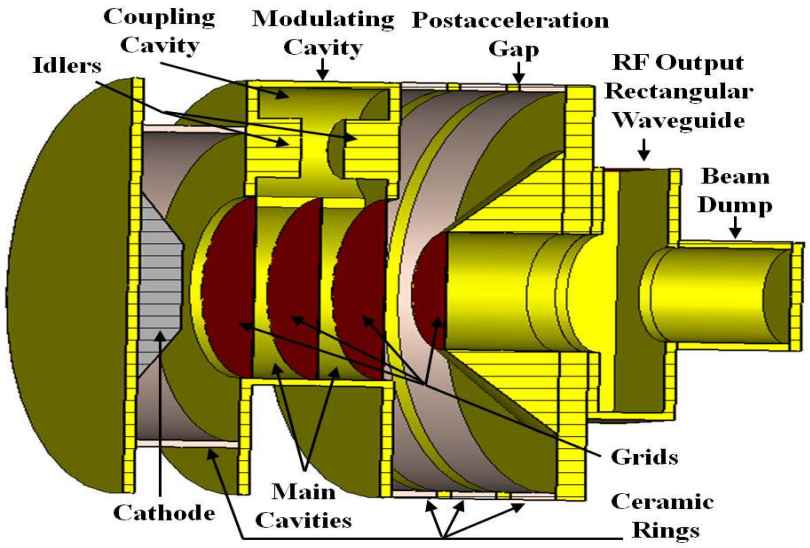

Figure 4.1: 3D schematic diagram of a reltron.

4.2. Analysis

In reltron oscillator, high DC voltage is applied at its cathode to excite the explosive emission electrons which results in the formation of plasma on the cathode surface. Due to this process, high current electron beam is generated and it helps further to establish the self-insulation condition in the device. The application of high DC voltage in the structure also perturbs the plasma due to the transient behaviour of the electromagnetic (EM) waves and the perturbed plasma oscillates with the plasma frequency. To understand the electron beam and EM wave interaction mechanism in the device, an analytical study is presented in this section.

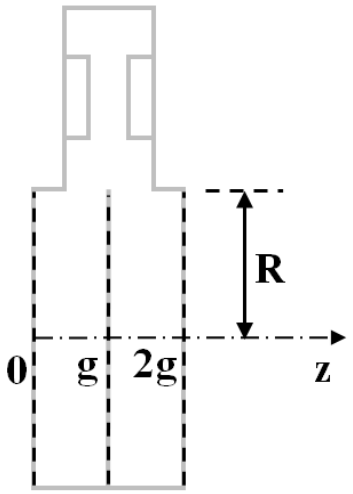

Figure 4.2: Basic schematic diagram of the modulation cavity of a reltron.

4.2.1. Bunching Field

The side-coupled modulation cavity of this device, as shown in Fig. 4.2, comprises of two main cavities and a coupling cavity to couple the EM fields between the main cavities. The main cavities consist of three grids placed in the front, middle and back (Fig. 4.2). Under the $\pi/2$ mode of operation, no field exists in the coupling

cavity while fields in the main cavities oscillate in opposite polarity. The RF electric field generated inside the modulation cavity in π/2 mode can be written as [Miller *et al*. (1992)]:

$$E = \begin{array}{ll} -E_0 \sin(\omega t + \theta) & 0 < z < g \\ E_0 \sin(\omega t + \theta) & g < z < 2g \end{array}, \qquad (4.1)$$

where E_0 is the peak field amplitude, θ is the initial phase condition, and g is the grid spacing. The metal grids in the modulation cavity allow the electrons to pass through and confine the RF waves in between. Due to the reflections of the RF wave from the metal grids, only standing waves exist in between the metal grids and therefore, the axial electric field can be expressed as the summation of stationary wave harmonics, in the form [Lemke (1992)]:

$$E_z = \sum_{n=1}^{\infty} E_{zn} = \sum_{n=1}^{\infty} [A_n J_0\{\Gamma_n r\} + B_n Y_0\{\Gamma_n r\}] e^{i(\omega t - \beta_n z)}, \qquad (4.2)$$

where $\Gamma_n (= (k^2 - \beta_n^2)^{1/2})$ is the radial propagation constant, k is the free space propagation constant and β_n (= $n\pi/g$) is the axial propagation constant. Here, n (= 1, 2, 3…) represents the stationary wave modal number. The axial electric field (E_z) consists of forward and backward waves of the standing wave and expressions for these two waves can be written as:

$$E_z^f = \sum_{n=1}^{\infty} E_{zn}^f = \sum_{n=1}^{\infty} [A_n^f J_0\{\Gamma_n r\} + B_n^f Y_0\{\Gamma_n r\}] e^{i(\omega t - \beta_n z)}, \qquad (4.3)$$

$$E_z^b = \sum_{n=1}^{\infty} E_{zn}^b = \sum_{n=1}^{\infty} [A_n^b J_0\{\Gamma_n r\} + B_n^b Y_0\{\Gamma_n r\}] e^{i(\omega t + \beta_n z)}, \qquad (4.4)$$

where the superscript f and b refer to the forward and backward components of the RF wave, respectively. The net axial electric field can be written as:

$$E_{zn} = E_{zn}^{f} + E_{zn}^{b} \ . \tag{4.5}$$

The axial electric field becomes null at the metal grid boundaries ($z = 0$, g, $2g$ (Fig. 4.2)) and $z = 0$ corresponds to the right face of the first grid and the wave equation can be written in the following form:

$$(E_{zn}^{f} + E_{zn}^{b})_{z=0} = (A_n^{f} + A_n^{b}) J_0\{\Gamma_n r\} + (B_n^{f} + B_n^{b}) Y_0\{\Gamma_n r\} = 0 \ ,$$

which, in view of $J_0\{\Gamma_n r\}$ and $Y_0\{\Gamma_n r\}$ each taking on finite values inside the main cavities, yields:

$$A_n^{b} = -A_n^{f} \text{ and } B_n^{b} = -B_n^{f} \ .$$

Further, the field components also become null at $r = R$ which refer to the metallic surface of the RF cavities enabling us to write:

$$B_n^{f} = -A_n^{f} \frac{J_0\{\Gamma_n R\}}{Y_0\{\Gamma_n R\}} \ . \tag{4.6}$$

Substituting (4.3) and (4.4) in (4.5) gives:

$$E_{zn} = -2i \sin(\beta_n z)[A_n^{f} J_0\{\Gamma_n r\} + B_n^{f} Y_0\{\Gamma_n r\}] e^{i\omega t} \tag{4.7}$$

and again substituting (4.6) in (4.7) yields:

$$E_{zn} = \sum_{n=1}^{\infty} A_n^{*} \mathrm{G}_n\{\Gamma_n r\} \sin(\beta_n z) e^{i\omega t} \ , \tag{4.8}$$

where $A_n^{*} = \dfrac{-2iA_n^{f}}{Y_0\{\Gamma_n R\}}$ and $\mathrm{G}_n\{\Gamma_n r\} = [J_0\{\Gamma_n r\} Y_0\{\Gamma_n R\} - J_0\{\Gamma_n R\} Y_0\{\Gamma_n r\}]$.

The electrons emitted through a field cathode under explosive emission condition enter the modulation cavity of the device which consists of two RF interaction cavities (main cavities) (Fig. 4.1). Here, these dense electrons interact with the RF

electric field present in the cavities which leads to the generation of space charge waves. Further, the electrons get velocity modulated in the first grid spacing then again in the second grid spacing, hence, twice in the modulation cavity, as a whole, which result in intense beam bunching. Therefore, the axial electric field including the effect of space charge wave can be written as [Levush *et al*. (1992)]:

$$E_{zn} = \begin{cases} \frac{1}{2}[G_n\{\Gamma_n r\}\,\zeta\{z,t\} + E_{scz}]\sin(\beta_n z)\; e^{i\omega t} & 0 \le z \le g \\ -\frac{1}{2}[G_n\{\Gamma_n r\}\,\zeta\{z,t\} + E_{scz}]\sin(\beta_n z)\; e^{i\omega t} & g \le z \le 2g \end{cases}, \tag{4.9}$$

where $\zeta\{z,t\}$ is the slowly varying amplitude of the RF wave. It is assumed that the slowly varying function varies in the axial direction and vanishes on the metal grid boundaries (z = 0, g, 2g (Fig. 4.2)). The slowing varying amplitude of the RF wave for the cylindrical cavity can be obtained by solving Maxwell's Faraday's and Ampere's law expressions and can be written in the form [Levush *et al*. (1992), Ding (1996)]:

$$\frac{d\zeta}{dt} + v\frac{d\zeta}{dz} = -\frac{1}{U}\int_0^{2g} dz \int_0^{R} 2\pi r dr\; G_n^{*}.j\sin(\beta_n z)\; e^{i\omega t},$$

where v is the velocity of electrons, U is the electromagnetic energy and j is the current density of the electron beam. The electrons are guided by the self- magnetic field of the cavity and electrons are propagating in the axial direction. Then, the phase of the beam is characterized by $\beta_n z - \omega t$. If the axial propagation constant (β_n) is fall in the range $0 \le \beta_n \le \beta_0 = 2\pi / g$, where g is the grid spacing , then the current density (j) becomes a factor of phase as $je^{\beta_n z - \omega t}$. With these assumptions and considering the effect of space charge waves following relationships are obtained as [Levush *et al*. (1992), Ding (1996)]:

$$\frac{d\zeta}{dt} + v\frac{d\zeta}{dz} = -\frac{1}{2}\frac{e}{mc^2} v(G_n\{\Gamma_n r\}\zeta\{z,t\} + E_{scz}) \sin(\beta_n z)\ e^{i\omega t},$$

and

$$\frac{i\omega}{c} E_{scz} \simeq \frac{4\pi}{c} j \sin(\beta_n z)\ e^{i\omega t}\ .$$

Using the above expressions, the axial electric field of space charge wave E_{scz} in the individual cavities of the modulation cavity (Fig. 4.1) can be obtained following the approach given in [Levush *et al*. (1992), Ding (1996)] as:

$$E_{scz} = \frac{\gamma^3 / \omega_p^2 (\beta_n v - \omega)^2}{1 - \gamma^3 / \omega_p^2 (\beta_n v - \omega)^2} G_n\{\Gamma_n r\}\zeta\{z,t\}\ ,$$

where ω_p is the plasma frequency, $\gamma\,(=(1-v^2/c^2)^{-1/2})$ is the relativistic mass factor. Here, e and m are electron charge and mass, respectively, and c is the speed of light. For the side coupled modulation cavity, the above expression modifies as:

$$E_{scz} = (\psi - 1)\, G_n\{\Gamma_n r\}\zeta\{z,t\}\ , \tag{4.10}$$

where, $\psi = \dfrac{\gamma^3}{\omega_p^2}\left(\dfrac{1}{(\beta_n v - \omega)^2} + \dfrac{1}{(\beta_n v + \omega)^2}\right)^{-1}$.

Now, putting this value of space charge wave E_{scz} in equation (4.9) and E_{zn} becomes:

$$E_{zn} = \begin{cases} \dfrac{\psi}{2} G_n\{\Gamma_n r\}\zeta\{z,t\}\sin(\beta_n z) e^{i\omega t} & 0 \le z \le g \\ -\dfrac{\psi}{2} G_n\{\Gamma_n r\}\zeta\{z,t\}\sin(\beta_n z) e^{i\omega t} & g \le z \le 2g \end{cases}. \tag{4.11}$$

The above expression for the axial stationary harmonic electric field is a combination of the standing and space-charge waves generated inside the cavity, thereby denotes the bunching field in the modulation cavity.

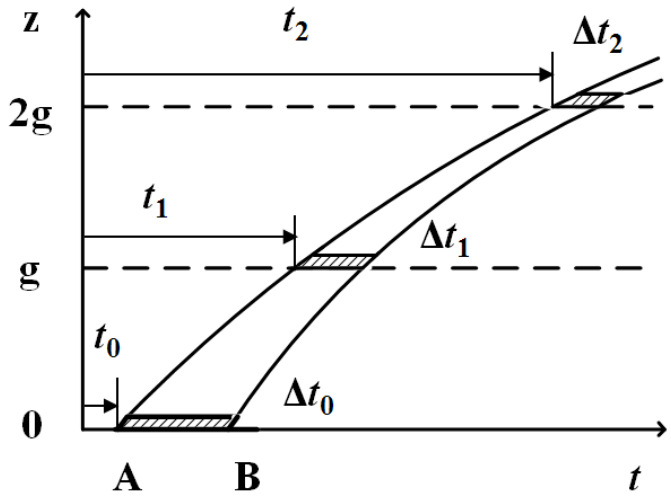

Figure 4.3: Electron Trajectories of two electrons A and B in presence of DC potential in the modulation cavity.

4.2.2. Modulation Process

In reltron, the beam bunching is performed in the longitudinal direction. Due to the rapid growth rate and high saturated electric field present, the beam current exceeds the space charge limiting current. This will depress the potential within the beam with respect to the electrode potential, and electrons stop moving further. Thus, as a consequence, a deep potential well is formed known as the virtual cathode. During the bunching phase, the virtual cathode moves in the opposite direction to the beam propagation leading to enhance electron densities. This process transforms the electron beam velocity modulation into density modulation in the very short distance of grid spacing of the modulation cavity. The beam bunching is also influenced by the self-electric fields of the electrons, and at a high current level, a potential hill is generated through which the electrons are moving [Friedman *et al.* (1984), Friedman *et al.* (1988)].

Considering an electron A, shown in Fig. 4.3, enters the modulation cavity $z = 0$ at time t_0 with initial velocity v_0 and leaves the first gap at time t_1 with the velocity [Soh *et al*. (2012)]:

$$v_1 = v_0\left[1+\frac{MV_{gap1}}{2V_{ak}}\sin(\beta_n z-\omega t_1)\right], \tag{4.12}$$

where V_{ak} is the cathode voltage, $M(=\sin(\omega g/v_0)/(\omega g/v_0))$ is the coupling coefficient and v_0 is the initial velocity of the electrons due to the cathode potential (V_{ak}). Here, V_{gap1} is the RF potential developed across the first grid spacing (Fig. 4.1), due to the space charge electric field, given by expression (4.11). Then, from the conservation of energy the electron A will leave the second gap at time t_2 with velocity:

$$v_2 = v_1\left[1+\frac{MV_{gap2}}{2(V_{ak}+V_{gap1})}\sin(\beta_n z-\omega t_2)\right] \tag{4.13}$$

where V_{gap2} is the RF potential developed across the second grid spacing. As the bunched electrons come out from the modulation cavity and enter in the post acceleration gap (Fig. 4.1), due to the applied acceleration potential V_{pa} in this region, the electrons bunches get re-accelerated and moves toward the extraction cavity with the velocity v_{pa}:

$$v_{pa} = v_2\left(1+\frac{V_{pa}}{V_{ak}+V_{gap1}+V_{gap2}}\right)^{1/2} \approx v_2\left(1+\frac{V_{pa}}{V_{ak}}\right)^{1/2}.$$

where V_{pa} is the post-acceleration voltage. Further, it could be appreciated from the above expression that the acceleration in this region causes all the electrons to propagate at the constant speed, approximately equal of the speed of light. This process in turn also increase the beam power.

To illustrate how a velocity modulation is converted into the density modulation in presence of DC potential, a theoretical description is shown in Fig. 4.3. Now, considering an electron beam which is velocity modulated in the 1st and 2nd grids spacings with velocities $v = v_0 + v_1\{t\}$ and $v = v_1 + v_2\{t\}$, respectively. Here, v_1 is the initial velocity of electrons entering the 2nd gap. In the π/2 mode of operation, the RF phase in the main cavities is in opposite polarity. The influence of deceleration / acceleration potential on the electron bunching can be seen from Fig. 4.3. In the first grid spacing $0 < z < g$ of the modulation cavity, the deceleration (d_0) is given as [Friedman *et al*. (1988)]:

$$d_0 \cong -\left|\frac{eE_{zn}}{\gamma^3 m}\right| .$$

Here, E_{zn} can be obtained from expression (4.11) and at $z = 0$, the initial velocity of all the electrons are constant, and at this point the deceleration (d_0) also becomes constant. As the electron propagates through the modulation cavity, the velocity of the electron changes and the relativistic mass factor is also changed. The change in the relativistic mass factor vary the deceleration d_0 in the cavity.

The electron A reaching $z = 0$ at time t_0 will arrive $z = g$ at time t_1 which can be obtained from:

$$g = [v_0 + v_1\{t_0\}](t_1 - t_0) - \frac{1}{2} d_0 (t_1 - t_0)^2 . \qquad (4.14)$$

Now considering further, another electron B, shown in Fig. 4.3, will arrive $z = g$ at time $t_1 + \Delta t_1$ which is to be computed from:

$$g = [v_0 + v_1\{t_0 + \Delta t_0\}][(t_1 + \Delta t_1) - (t_0 + \Delta t_0)] - \frac{1}{2} d_0[(t_1 + \Delta t_1) - (t_0 + \Delta t_0)]^2 , \quad (4.15)$$

Equation (4.14) and (4.15), yields:

$$\Delta t_1 = \Delta t_0 \left(1 + \frac{g}{{v_0}^2} \mathcal{F} \frac{\partial v_1\{t_0\}}{\partial t_0} \right) , \quad (4.16)$$

where $\mathcal{F} \cong \frac{2}{X}\left(\frac{1}{\sqrt{1-X}} - 1 \right)$ is the field enhancement factor and $X \cong 2\left| eV_{ak} \right| / mc^2 \gamma^3 \beta_n^2$ is the normalized static potential.

Considering now the charge conservation in the 1st grid spacing [Friedman *et al.* (1988)]:

$$I_0 \Delta t_0 = (I_0 + I_1)\Delta t_1 \quad (4.17)$$

and using (4.16) in (4.17) becomes:

$$I_1 \cong -\frac{I_0 g}{{v_0}^2} \mathcal{F} \frac{\partial v_1\{t_0\}}{\partial t_0} , \quad (4.18)$$

which is the current modulation at $z = g$ under the influence of retarding potential. Since, both the main cavities of the modulation cavity are identical in nature, therefore, in the second grid spacing $g < z < 2g$, there is an accelerating electric field of same magnitude that of the retarding field as in case of first grid spacing. Hence, the current modulation at z = 2g becomes:

$$I_2 \cong -\frac{I_1 g}{\tilde{v}_0^{\,2}} \mathcal{F} \frac{\partial v_2\{t_1\}}{\partial t_1} . \quad (4.19)$$

This equation represents the conversion of velocity modulation into current modulation in the side coupled modulation cavity.

4.2.3. Associated RF Energy

For an optimum electron beam and RF wave interaction in reltron, the space charge waves are synchronized with the electron beam. A realistic model of reltron is shown in Fig. 4.1 in which all the electrons in the beam is assumed to have the same constant values of energy (*H*) and canonical momentum ($\hat{p}_z$). The corresponding electric field profile distribution function is defined as [Lemke *et al*. (1992)]: [11]

$$f_0\{r, p\} = \eta\{r\}\,\delta\{H - mc^2 + c\hat{p}_z\}\,\delta\{p_r\}\,\delta\{p_\theta\}\ , \tag{4.20}$$

where $\eta\{r\}$ represents the charged particle density and δ represents the Dirac delta function. The terms p_r and p_θ are the radial and azimuthal component of the momentum (*p*), respectively. The Dirac delta function is defined as:

$$\int_{-\infty}^{\infty} \delta(x)dx = 1\,,$$

which enables us to write:

$$\int_{-\infty}^{\infty} \delta\{H - mc^2 + c\hat{p}_z\}dr = 1\,.$$

Using the law of conservation of energy, the total sum of the charge particles energies becomes zero and can be expressed as [Lemke *et al*. (1992)]:

$$H = c\{p_z^2 + m^2c^2\}^{1/2} - e\phi\{r\}\ , \tag{4.21}$$

where $\phi\{r\}$ is the electrical potential. In case of reltron, the canonical momentum ($\hat{p}_z$) can be obtained as [Garrison and Chiao (2004)]:

$$\hat{p}_z = p_z - e\,B_z\{r\}/c\,,$$

where p_z is the axial momentum and $B_z\{r\}$ represents the equilibrium magnetic potential. The density of charged particles can be expressed in the form [Lemke *et al*. (1992)]:

$$\eta\{r\} = K^2 (mc^3 / 4\pi e^2)(r_c / r)^K / r^2 ,$$

where $K = I_A / (\gamma I_\alpha)$ and $I_\alpha = mc^3 / 2e$. I_A is the anode current given by the expression (4.19). To find the electric and magnetic potentials, Poisson's equation ($\nabla^2 \phi\{r\} = -\rho / \varepsilon_0$), Maxwell's Ampere's law ($\nabla \times B = \mu_0 j + (1/c^2)\partial E / \partial t$) and current density ($j = \rho v$) are used to get the final expression in terms of second order differential equations as:

$$\frac{\partial^2}{\partial r^2}\phi\{r\} = -4\pi\rho\{r\} , \tag{4.22}$$

$$\frac{\partial^2}{\partial r^2} B_z\{r\} = -\frac{4\pi}{c} j_z\{r\} , \tag{4.23}$$

where $\rho\{r\}$ and $j_z\{r\}$ is the space charge and current densities, respectively. The charge and current densities of the cavity can be defined as:

$$\rho\{r\} = -e \int_{-\infty}^{\infty} \int_{-\infty}^{\infty} \int_{-\infty}^{\infty} dp_z dp_\theta dp_r f_0\{r, p\} , \tag{4.24}$$

and

$$j_z\{r\} = -e \int_{-\infty}^{\infty} \int_{-\infty}^{\infty} \int_{-\infty}^{\infty} dp_z dp_\theta dp_r v_z f_0\{r, p\} . \tag{4.25}$$

Substituting (4.20) in (4.24) and (4.25) provides:

$$\rho\{r\} = -(mc^2 / 4\pi e)(K / r)^2 \cosh(\chi) , \tag{4.26}$$

and

$$j_z\{r\} = -(mc^3 / 4\pi e)(K / r)^2 \sinh(\chi) , \tag{4.27}$$

where $\chi = \ln[(r_m / r_c)^K]$. Here, r_m and r_c are main cavity and cathode radii, respectively. The corresponding equilibrium potentials of the cavity can be obtained using equations (4.22) - (4.25) as:

$$e\phi\{r\} = mc^2[\cosh(\chi) - 1] \ , \tag{4.28}$$

and

$$eB_z\{r\} = mc^2 \sinh(\chi) \ . \tag{4.29}$$

The electron drift velocity along the longitudinal direction is now obtained by dividing (4.27) to (4.26) as:

$$v_z\{r\} / c = \tanh(\chi) \ . \tag{4.30}$$

After the post-acceleration, all the electron bunches pass the post-acceleration gap at a constant speed, nearly equal to the speed of light. This phenomenon maintains the relative positions between the electrons bunches which help in reducing the relative kinetic energy spread. Further, it also increases the beam energy and efficiency of the device [Miller *et al*. (1992)].

4.3. Particle Simulation Description

As To predict the electromagnetic behavior of the RF cavity as well as beam-wave interaction process in the reltron (Fig. 4.1), the device is simulated using commercial PIC simulation code "CST Particle Studio". For the beam wave interaction simulation, the device is modeled as per the design methodology described in the previous chapters. To ensure the desired mode excitation and resonating frequency in the modulation cavity, Eigenmode simulation is performed in the absence of the electron beam. Once the operating mode and frequency are confirmed, the complete

structure is designed. In the simulation model, the post-acceleration gap is made of stacks of alternating plastic insulator rings and metal rings. To emit the electrons from the cathode, explosive emission condition is evoked. A waveguide port is assigned at the output cavity to observe the RF output power. Discrete ports are used to apply the cathode voltage, post-acceleration voltage, and initial beam current. The background material is kept normal (vacuum). In order to analyze the structure using simulation code various boundary conditions need to be satisfied to provide solutions in a region of finite dimensions. The boundary condition, tangential electric field null at the metal boundaries ($E_t = 0$) is applied in all directions. The detailed design specifications of reltron are listed in Table 4.1. Once the structure is modeled, the beam present simulation is performed to observe the oscillation frequency, RF output power and efficiency of the device.

Table 4.1: Design specification of reltron.

Parameters	Value
Operating frequency	2.75 GHz
Initial Beam Current	750 A
Cathode voltage (V_{ak})	100 kV
Post-acceleration voltage (V_{pa})	750 kV
Main cavity radius	38.27 mm
Coupling cavity radius	25.51 mm
Idler radius	12.75 mm
Grid spacing (g)	18.70 mm
A-K gap spacing	20.50 mm
Post-acceleration gap	53.30 mm

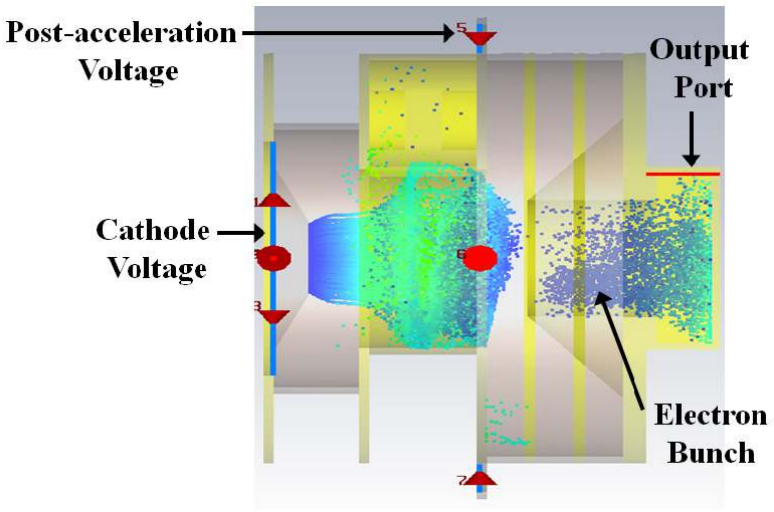

Figure 4.4: Simulated reltron structure model and electrons' position obtained during the PIC simulation.

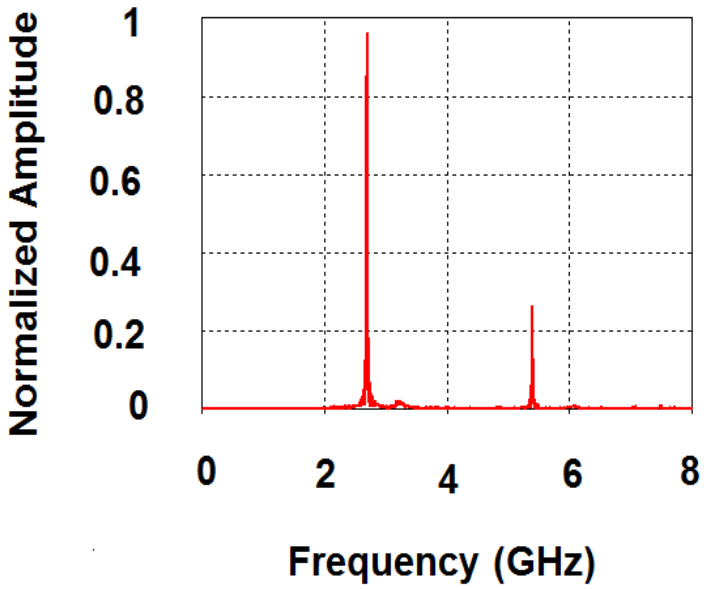

Figure 4.5: Frequency spectrum at the output port of the device.

The anode-cathode gap and the post-acceleration gap are driven by 100 kV and 750 kV DC potentials, respectively with 1ns rise time. The initial beam current applied at the cathode is set at 750 A. With these specifications, the beam present simulation is performed for 100 ns duration. The electron's phase space obtained during the PIC simulation is shown in Fig. 4.4. The electrons emitted from the cathode surface due to

the explosive emission process enter the modulation cavity. The electrons are under space charge limited condition between the grids of the modulation cavity results in the virtual cathode formation which helps in the velocity modulation. As shown in Fig. 4.4, the beam bunching is occurring in the modulation cavity, and the bunch is reaccelerated through the post-acceleration gap. The accelerated bunch is separated from the remaining bunches and moves towards the extraction cavity. The frequency spectrum obtained at the output port of the device is plotted as Fig. 4.5, which indicates that the operating frequency of the reltron is ~2.75 GHz.

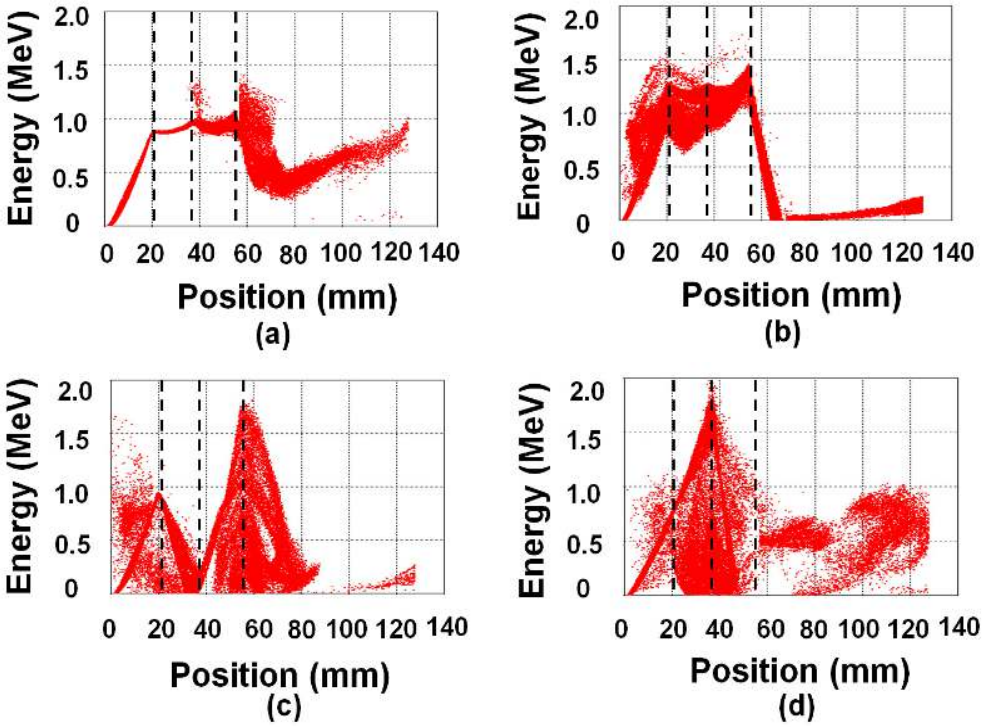

Figure 4.6: Plot of electrons' kinetic energy at (a) 3 ns (b) 4 ns (c) 11 ns (d) 12 ns time during the PIC simulation of the reltron.

The electron's kinetic energy distribution of reltron is shown in Fig. 4.6 at the different time intervals. Three grids of the modulation cavity are indicated with the dotted line. Before the onset of oscillation, the electrons are not optimally bunched and are shown in Figs. 4.6 (a) and (b) at 3 ns and 4 ns time durations, respectively. Once the

oscillation is set up, in the first half cycle the electrons decelerate in the first grid spacing and accelerate in the second grid spacing as shown in Fig. 4.6(c). In the second half cycle, a reverse process takes place due to the Lorentz reversal force, as can be also seen in Fig. 4.6(d). This acceleration and deceleration processes give a continuous double velocity modulation resulting in the highly bunched beams coming out from the modulation cavity which has very large energy spread and is eliminated by the application of post-acceleration voltage in the device.

4.4. Results and Discussion

Reltron is a highly efficient HPM source and the current developed in the side-coupled modulation cavity is high enough to establish the self-magnetic condition. Starting from the basic principles, expressions for the bunching field, modulation process and the associated RF energy developed have been discussed. In order to validate the analytical approach developed PIC code "CST Particle Studio" has been used.

The axial electric field (E_{zn}) in the modulation cavity is obtained using the expression (4.11) and is plotted as Fig. 4.7. Here, the parameters chosen for the numerical calculation is listed in Table 4.1. This RF electric field is responsible for the bunching of electrons and energy transfer in the device. The RF electric fields in both the grid spacing increase with the cavity length and attain a maximum value at the centre of the cavity and again reach to the minimum at the grids, which leads to a stronger beam bunching. Further, the two high RF field peaks of equal magnitude in each grid spacing show a double velocity modulation of electrons in the modulation cavity. The RF electric field obtained using PIC simulation in the modulation cavity is also plotted in Fig. 4.7, which is similar in nature to the analytical field. To get an

overview of the formation of the electron bunches in the modulation cavity, a distance-time plot has been shown in Fig. 4.8. Here, the electron starts moving closer to each other with modulation cavity distance and at end of the modulation cavity intense bunching is formed. After the modulation cavity, the electron bunches would experience a large energy spread which is eliminated with the application of post-acceleration voltage.

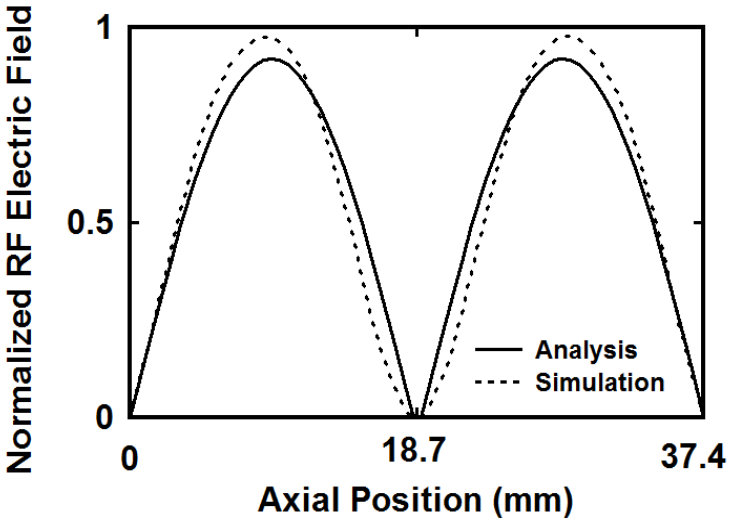

Figure 4.7: Variation of the normalized RF electric field along the axial direction in the side-coupled modulation cavity.

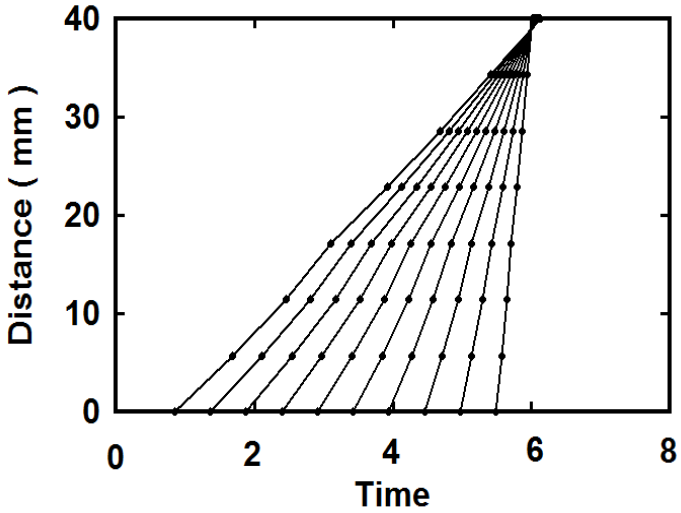

Figure 4.8: Distance-time graph for the electron beam movement in the side-coupled modulation cavity.

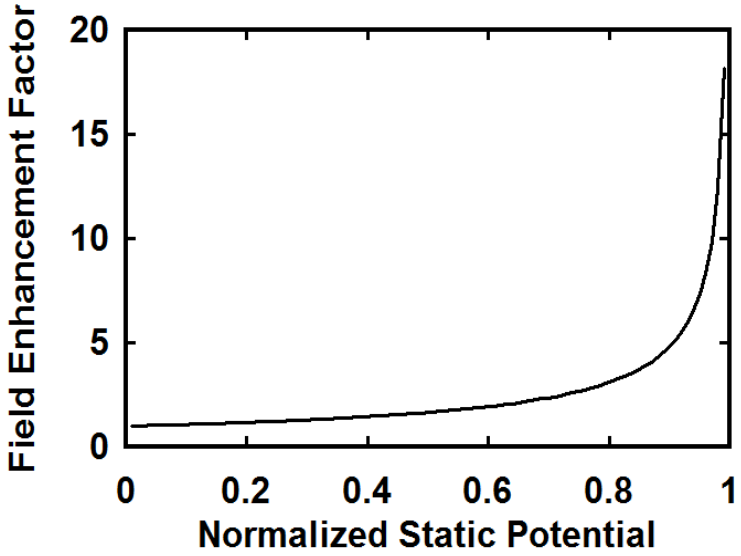

Figure 4.9: Field enhancement factor as a function of normalized static potential in the side-coupled modulation cavity.

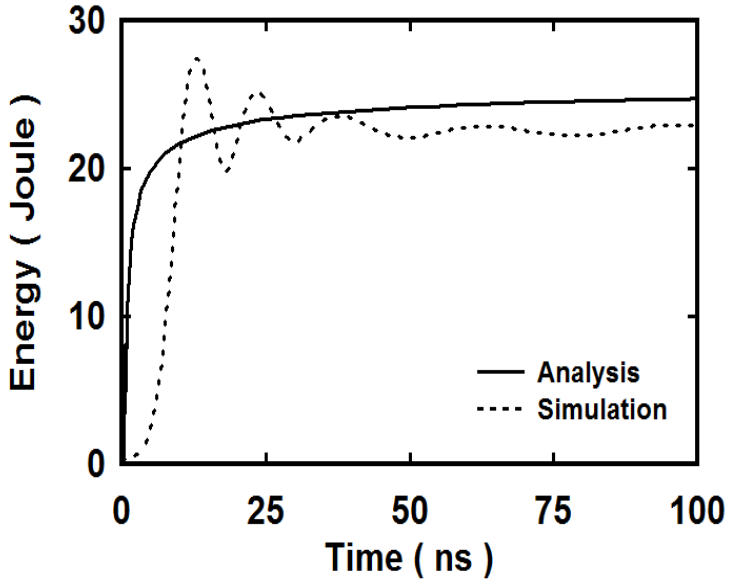

Figure 4.10: RF energy developed in the reltron, for the typically selected device parameters, Table 4.1.

The dependence of field enhancement factor ($\mathcal{F}$) on the normalized static potential (X), is shown in Fig. 4.9. For the small values of X, $\mathcal{F}$ is nearly unity. The field enhancement factor varies only with the potential barrier and is independent of the

distance over which the electrons are decelerated. The influence of DC potential on the current modulation can be seen from Fig. 4.3. In the first grid spacing $0 < z < g$ where a retarding potential is present, the electron B has a higher velocity than electron A and electron B will take less time to reach $z = g$ than electron A, which increases the current modulation. In the second grid spacing $g < z < 2g$, the same enhancement in the current modulation takes place, if the accelerating field is of the same magnitude as that of the retarding field in the first grid spacing.

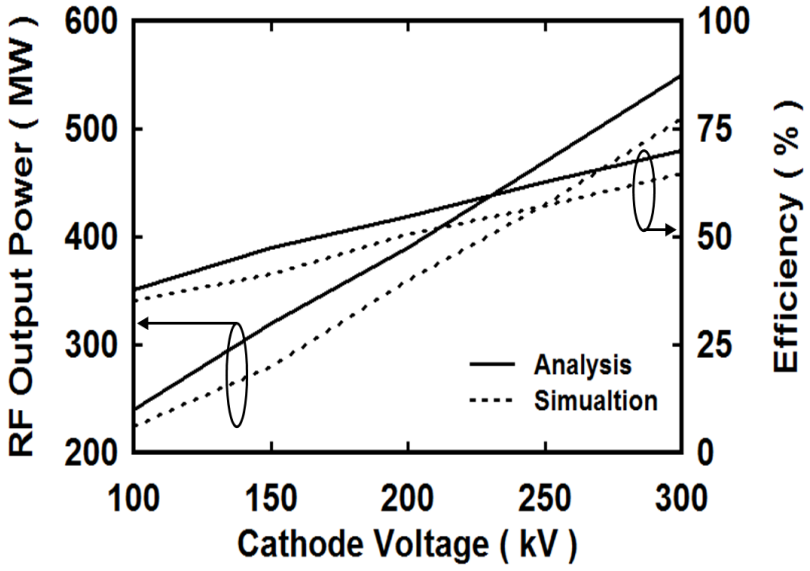

Figure 4.11: RF output power and the electronic efficiency of the reltron, as function of cathode voltage, for the typically selected device parameters, Table 4.1.

The RF energy growth of the reltron oscillator can be computed using the expression (4.21) for 2.75 GHz frequency, and it is found to be ~24 Joule for 100 ns pulse duration, as shown in Fig. 4.10 (for the device parameters listed in Table 4.1). It can be seen from Fig. 4.10 that for the typical device selected gives a stable RF output in around 12 ns time duration. Further, RF energy released is used to calculate the corresponding RF output power and efficiency of the device. With the beam parameters

listed in Table 4.1, the RF energy obtained through PIC simulation is ~22.5 Joule for a pulse duration of 100 ns is shown in Fig. 4.10.

The corresponding RF output power from the analytical calculation and PIC simulation are ~240 MW with ~38% efficiency and ~225 MW with ~36% efficiency, respectively, for the typically selected reltron device (listed in Table 4.1): total beam voltage = 850 kV, cathode voltage = 100 kV, post-acceleration voltage = 750 kV and initial beam current = 750 A. With these beam parameters, Miller *et al*. [Miller *et al*. (1992)] have obtained an RF output power of 200 MW with ~32% efficiency. The analytical and PIC simulation results obtained are in agreement with the experimental results of Miller *et al*. [Miller *et al*. (1992)] within ~6%.

The parametric analysis is also carried out to study the sensitivity of the device on the cathode voltage using PIC simulation as well as the analytical study. The RF output power and efficiency of the device as a function of cathode voltage with a static post-acceleration voltage of 750 kV and the initial beam current of 750 A, have shown in Fig 4.11. At higher cathode voltage, the RF output power and efficiency of the device increases, due to the stronger beam bunching in the modulation cavity. The PIC simulation of reltron provides a maximum RF output power of ~510 MW with ~64% efficiency while the analytical study gives a maximum RF output power of ~550 MW with ~70% efficiency when the cathode voltage is set at 300 kV. Hence, the performance of the device can be improved by increasing the cathode voltage. The computed RF output power values of the reltron device obtained through the present analysis is found to be in agreement with the PIC simulation results within 6%.

4.5. Conclusion

An analytical description is presented in this chapter to develop insight of the beam wave interaction process of the reltron oscillator. The RF electric field developed in the modulation cavity of the device is obtained using the split cavity oscillator principle. Relativistic klystron analysis has been extended here to describe the electron beam modulation process in the side coupled modulation cavity used in the reltron. The analysis has been extended further to obtain the RF energy growth which is used to evaluate the RF output power and efficiency of the device. The analytical approach developed here for the reltron has got validated with a previously reported experimental work as well as the 3D PIC simulation of the device. For the selected beam parameters of experimental device with 100 kV cathode voltage, 750 kV post-acceleration voltage and 750 A beam current at 2.75 GHz frequency, the analytical and simulation results predicts RF output powers of ~240 MW with ~38% efficiency and ~225MW with ~36% efficiency, respectively, for 100 ns pulse duration. With the parametric variation, the analytical study provided maximum RF output power of ~ 550 MW with ~ 70% and with PIC simulation ~ 510 MW RF output power with ~64% efficiency when the cathode voltage was set at 300 kV, post-acceleration voltage at 750 kV and beam current at 750 A. The obtained analytical and simulation results are found in agreement of ~ 6% with the previously reported experimental values for RF output power and efficiency of the device. The parametric analysis suggested that the overall performance of the device increases at higher cathode voltage. It is hoped that this paper would be useful for the tube developer to evaluate the practical device as well as design and development of the reltron.